

Validation of EEG forward modeling approaches in the presence of anisotropy in the source space

F. Drechsler¹, J. Vorwerk², J. Haueisen³, L. Grasedyck⁴, and C. H. Wolters²

¹Max Planck Institute for Mathematics in the Sciences, Inselstr. 22, D-04103 Leipzig, Germany

²Institute for Biomagnetism and Biosignalanalysis, University of Münster, 48149 Münster, Germany

³Institute of Biomedical Engineering and Informatics, TU Ilmenau, POB 100565, D-98684 Ilmenau, Germany

⁴Institute for Geometry and Applied Mathematics, RWTH Aachen, Templergraben 55, D-52056 Aachen, Germany

E-mail: carsten.wolters@uni-muenster.de

Abstract. The quality of the inverse approach in electroencephalography (EEG) source analysis is — among other things — depending on the accuracy of the forward modeling approach, i.e., the simulation of the electric potential for a known dipole source in the brain.

Here, we use multilayer sphere modeling scenarios to investigate the performance of three different finite element method (FEM) based EEG forward approaches – subtraction, Venant and partial integration – in the presence of tissue conductivity anisotropy in the source space. In our studies, the effect of anisotropy on the potential is related to model errors when ignoring anisotropy and to numerical errors, convergence behavior and computational speed of the different FEM approaches. Three different source space anisotropy models that best represent adult, child and premature baby volume conduction scenarios, are used.

Major findings of the study include (1) source space conductivity anisotropy has a significant effect on electric potential computation: The effect increases with increasing anisotropy ratio; (2) with numerical errors far below anisotropy effects, all three FEM approaches are able to model source space anisotropy accordingly, with the Venant approach offering the best compromise between accuracy and computational speed; (3) FE meshes have to be fine enough in the subdomain between the source and the sensors that capture its main activity. We conclude that, especially for the analysis of cortical development, but also for more general applications using EEG source analysis techniques, source space conductivity anisotropy should be modeled and the FEM Venant approach is an appropriate method.

PACS numbers: 87.19.L, 87.19.R, 87.10.-e, 02.30.Dh

Keywords: EEG, source analysis, forward problem, finite element method, anisotropy, multilayer sphere models, validation

1. Introduction

In EEG and magnetoencephalography (MEG) source analysis, the inverse solution, i.e., the reconstruction of a current distribution in the brain from non-invasive measurements of the electric potential at the head surface, depends — among other things — on the accuracy of the forward problem [9, 22, 29]. For an appropriate solution of the forward problem it is important to keep both *model* and *numerical errors* as small as possible.

Model errors result, for example, from unrealistic or simplifying assumptions on head volume conductor geometry and tissue conductivity structure. In this paper, we will focus on the model error caused by ignoring tissue conductivity anisotropy in the source space (the brain grey matter compartment). After the volume conductor model has been determined, *numerical errors* of the chosen numerical method result from an insufficient discretization and approximation of the potential due to, for example, insufficient mesh resolution, bad (deformed) elements or an inappropriate choice of the basis functions with regard to the regularity of the solution function.

Different numerical methods have been proposed with the goal to solve the EEG and MEG forward problem in the presence of brain tissue conductivity anisotropy, under which are the finite difference method (FDM) [20, 35], the finite volume method (FVM) [12] and the finite element method (FEM). This paper focuses on the FEM which allows high accuracy for the numerical solution of elliptic partial differential equations since it is specifically tailored to the corresponding variational formulation [19, 8, 65, 16] and since it allows high flexibility and accuracy in modeling the forward problem in geometrically complicated inhomogeneous and anisotropic head volume conductors [5, 2, 56, 10, 30, 38, 59, 47, 60, 55, 18, 43, 42].

Recent studies investigated the influence of brain anisotropy in realistic head models [24, 62, 63, 21, 18]. It was found that, besides the non-negligible effects of the so-called *remote anisotropy* (anisotropy in a certain distance to the source), conductivity changes close or within the source space have an especially significant effect on the forward problem [62, 23]. However, to the best of our knowledge, a validation of FEM-based forward approaches in the presence of anisotropy in the source space has not yet been presented, and the relationship between model errors due to anisotropies in the source space and numerical errors remains unclear. The standard in source analysis is still the use of a homogenized isotropically conducting source space.

When using the effective medium approach, developed and validated in [3, 54, 36, 58], that relates conductivity tensors and water diffusion tensors in a linear way, brain conductivity anisotropy can be determined non-invasively by means of diffusion tensor magnetic resonance imaging (DT-MRI or DTI) techniques.

Using modern 7T MRI machines, evidence for grey matter anisotropy in adults was recently found in [25, 11]. In [25, Fig. 4], a fractional anisotropy (FA) map with overlaid vector-orientation showed a clear normally-oriented (radial) anisotropy in the cortex. In [26, Figure 39.7], this result is confirmed. It has thus been measured that the largest diffusion tensor eigenvalue is the one in radial direction. In [11, Fig. 4],

FA values in the range of up to 0.15 were measured for the area of the central sulcus, which would relate to an anisotropy ratio of about 1.3:1. FA-values were not constant in the region of interest; higher FA was measured in Broadman area BA4 (primary motor cortex) and lower in BA2 (sensory cortex). In [48], an anisotropy ratio of up to 1.41:1 (in the head of the caudate nucleus) was measured for adults. This ratio would relate to an FA value of approximately 0.21. This motivates our choice of a 1.41:1 (radial:tangential) conductivity anisotropy ratio for the grey matter compartment in our *adult model* described in detail later in this study. To the best of our knowledge, it is not likely that an even more pronounced source space anisotropy is realistic for the adult case.

However, the human brain undergoes a dramatic maturation during the first years of life. Both the grey and white matters change rapidly during the first two years of life as indicated by the changes in T1 contrast of the grey versus white matter around 6 to 9 months after birth [1]. In the period 26 to 29 weeks of gestation, a rapid dendritic differentiation in the cortical plate, the appearance of a six-layered pattern and a maximal development of the subplate zone has been reported [32]. As shown in [34, 33], the grey matter anisotropy ratio is increasing with decreasing age. Since the investigation of the cortical development using non-invasive EEG and MEG techniques is of increasing interest [17, 41, 39, 37, 45, 40, 27], a correct modeling of especially these higher levels of source space anisotropy might significantly contribute to an understanding of the observed maturation effects. In [34] and in [33, Fig. 2], anisotropy ratios have been measured in the cortex of premature babies of 26 weeks of gestational age, which could otherwise only be found in white matter tissue. Therefore, for our *premature baby* model described in detail in the methods section of this paper, we assume a source space anisotropy ratio of 5:1 as a representation of an upper limit of grey matter anisotropy in humans and for our *child model* a ratio of 2.7:1 ‡.

The three chosen cortical anisotropy ratios are upper limits of grey matter anisotropy and surely only rough approximations of the realistic situations, especially since they are known to vary strongly depending on the exact location in the grey matter compartment [48, 11]. The chosen ratios have to be seen in the light of the main interest of this study: We want to investigate relationships of grey matter anisotropy modeling errors and corresponding numerical errors. The goal is to gain deeper insight in the effects of cortical conductivity anisotropy on the EEG forward problem and to present the requirements with regard to a successful FEM modeling. Only if we can find FEM parametrizations which lead to numerical errors that are below the model errors, we can conclude that we model grey matter anisotropy accordingly. Since numerical errors can only be studied in simplified volume conductors, we restrict this study to multilayer-sphere models with constant radial and tangential conductivity values for the different tissue compartments, where quasi-analytical solutions exist [14].

‡ unpublished maximal cortical anisotropy ratio in a DTI study of a child

In the next section, we will shortly introduce the EEG forward problem and three different FEM approaches for the modeling of a current dipole in inhomogeneous and anisotropic volume conductors, the *subtraction approach* described in detail in [16, 65], the *Venant approach* introduced in [10] and described in detail in [61] and the *partial integration (PI)* approach [59, 55]. In our previous work [28], we compared all three approaches in tetrahedral volume conductors with isotropic source space, while, for the first time, we validate in the presence of cortical conductivity anisotropy here. We then describe our measures for model errors (or cortical anisotropy *effect errors*) and numerical errors and detail the setup of the volume conductor models. We optimize cortical conductivity values so that anisotropy effects are purely due to anisotropy and not to a suboptimal choice of the corresponding homogenized isotropic conductivity. Starting from a coarser mesh, we then generate globally and locally refined tetrahedral models to examine convergence behavior of the different FEM approaches. In the first two studies, the refined mesh models are constraint to fulfill the so-called *homogeneity condition* of the full subtraction approach, namely the condition that conductivity is not allowed to change in a small subdomain around the source (in our setup the tetrahedron of the coarsest mesh that contains the source). The result section is divided in three studies: The first and the second study, where globally refined and locally refined meshes are used, resp., have the goal to present the effect of cortical conductivity anisotropy in the three different volume conductor models, relate those effects to the numerical errors and determine the FEM approach that performs best with regard to numerical error, computational speed and constraints on mesh resolution and practical applicability. In the third study, the model error is further reduced by means of relaxing the homogeneity condition and the best-performing FEM approach of studies 1 and 2 is used for computation. In the last section, we discuss results and conclude.

2. Methods

2.1. Forward problem formulation

Assuming the quasi-static approximation of the Maxwell equations, the electric potential u in the head domain Ω with conductivity distribution σ , evoked by a primary current \mathbf{j}^p , is given by a Poisson equation with homogeneous Neumann boundary conditions on the head surface $\Gamma = \partial\Omega$. This can be expressed by

$$\nabla \cdot (\sigma \nabla u) = \nabla \cdot \mathbf{j}^p = J^p \text{ in } \Omega, \quad \langle \sigma \nabla u, \mathbf{n} \rangle = 0 \text{ on } \Gamma, \quad (1)$$

with \mathbf{n} being the unit surface normal. To achieve uniqueness of the solution a reference electrode with given potential has to be fixed, i.e., $u(\mathbf{x}_{ref}) = 0$ [46, 22, 65]. A primary current at position $\mathbf{y} \in \mathbb{R}^3$ and with moment $\mathbf{M} \in \mathbb{R}^3$ is represented by a mathematical dipole

$$J^p(\mathbf{x}) = \nabla \cdot \mathbf{j}^p(\mathbf{x}) = \nabla \cdot (\mathbf{M} \cdot \delta(\mathbf{x} - \mathbf{y})), \quad (2)$$

where δ is the Dirac delta distribution [46, 15, 22, 65].

2.2. Finite element method

We discretize (1) using a variational formulation and a Galerkin FE approach. We choose linear basis functions φ_i at the vertex positions ξ_i , $i \in \{1, \dots, N\}$, of a discretization of Ω . The finite element approach leads to the following linear equation system

$$Ku = b^y, \quad K \in \mathbb{R}^{N \times N}, \quad u, b^y \in \mathbb{R}^N \quad (3)$$

[65, 16] with the stiffness matrix

$$K_{ij} := \int_{\Omega} \langle \sigma(\mathbf{x}) \nabla \varphi_j(\mathbf{x}), \nabla \varphi_i(\mathbf{x}) \rangle d\mathbf{x}, \quad i, j \in \{1, \dots, N\},$$

and the right-hand side

$$b^y := - \int_{\Omega} J^p(\mathbf{x}) \varphi_i(\mathbf{x}) d\mathbf{x} = - \int_{\Omega} \nabla \cdot \mathbf{j}^p(\mathbf{x}) \varphi_i(\mathbf{x}) d\mathbf{x}. \quad (4)$$

2.3. Dipole models

As described in the introduction, we evaluate three different FE approaches for the treatment of the singularity on the right hand side (4) with regard to their performance in the presence of source space anisotropy. In the following, we will give a short overview of their derivations.

2.3.1. Subtraction approach Under the assumption that there exists a non-empty open neighborhood Ω_{∞} of the source position \mathbf{y} with constant (possibly anisotropic) conductivity $\sigma^{\infty, \mathbf{y}} := \sigma(\mathbf{y}) \in \mathbb{R}^{3 \times 3}$, we split up the potential u and the conductivity σ into the parts

$$u = u^{corr, \mathbf{y}} + u^{\infty, \mathbf{y}}, \quad (5)$$

$$\sigma = \sigma^{corr, \mathbf{y}} + \sigma^{\infty, \mathbf{y}}. \quad (6)$$

Here, $u^{\infty, \mathbf{y}}$, the so-called *singularity potential*, is the analytical solution for a dipole in an unbounded homogeneous conductor with constant (possibly anisotropic) conductivity $\sigma^{\infty, \mathbf{y}}$, which can be computed as

$$u^{\infty, \mathbf{y}}(\mathbf{x}) := \frac{1}{4\pi \sqrt{\det \sigma(\mathbf{y})}} \frac{\langle \mathbf{M}(\mathbf{y}), \sigma(\mathbf{y})^{-1}(\mathbf{x} - \mathbf{y}) \rangle}{\langle \sigma(\mathbf{y})^{-1}(\mathbf{x} - \mathbf{y}), \mathbf{x} - \mathbf{y} \rangle^{3/2}}. \quad (7)$$

$u^{corr, \mathbf{y}}$ is the so-called *correction potential* that solves the equation

$$\nabla \cdot (\sigma \nabla u^{corr, \mathbf{y}}) = f(\mathbf{x}) \text{ in } \Omega, \quad (8)$$

$$\langle \sigma \nabla u^{corr, \mathbf{y}}, \mathbf{n} \rangle = g(\mathbf{x}) \text{ on } \Gamma \quad (9)$$

with

$$f(\mathbf{x}) := \nabla(\sigma(\mathbf{y}) - \sigma(\mathbf{x})) \nabla u^{\infty, \mathbf{y}}(\mathbf{x}) \quad \text{for } \mathbf{x} \in \Omega \quad (10)$$

$$g(\mathbf{x}) := -\langle \sigma(\mathbf{x}) \nabla u^{\infty, \mathbf{y}}(\mathbf{x}), \mathbf{n}(\mathbf{x}) \rangle \quad \text{for } \mathbf{x} \in \Gamma \quad (11)$$

and is computed numerically. Applying the FE method, we obtain the right hand side

$$\begin{aligned} b_i^{\mathbf{y}} &:= \int_{\Omega} \langle (\sigma(\mathbf{y}) - \sigma(\mathbf{x})) \nabla u^{\infty, \mathbf{y}}(\mathbf{x}), \nabla \varphi_i(\mathbf{x}) \rangle d\mathbf{x} \\ &\quad - \int_{\Gamma} \varphi_i(\mathbf{x}) \langle \mathbf{n}(\mathbf{x}), \sigma(\mathbf{y}) \nabla u^{\infty, \mathbf{y}}(\mathbf{x}) \rangle d\Gamma, \quad i \in \{1, \dots, N\} \end{aligned} \quad (12)$$

and, after solving (3) with right hand side (12) for the correction potential, we obtain the approximated solution for the total potential

$$u(\mathbf{x}) = \sum_{i=1}^N (u_i + u^{\infty, \mathbf{y}}(\xi_i)) \varphi_i(\mathbf{x}).$$

We refer to [16, 65] for more detailed mathematics of the subtraction approach, where a proof for existence and uniqueness and statements about convergence properties can be found.

2.3.2. Partial integration approach Applying partial integration to (4) gives us

$$- \int_{\Omega} (\nabla \cdot \mathbf{j}^p) \varphi_i d\mathbf{x} = \int_{\Omega} \langle \mathbf{j}^p, \nabla \varphi_i \rangle d\mathbf{x} - \int_{\Gamma} \langle \mathbf{j}^p, \mathbf{n} \rangle d\Gamma.$$

We exploit the fact that the current density vanishes on the head surface and achieve

$$- \int_{\Omega} (\nabla \cdot \mathbf{j}^p) \varphi_i d\mathbf{x} = \int_{\Omega} \langle \mathbf{j}^p, \nabla \varphi_i \rangle \stackrel{(2)}{=} \langle \mathbf{M}, \nabla \varphi_i(\mathbf{y}) \rangle. \quad (13)$$

This gives us the right hand side for the partial integration approach

$$b_i^{\mathbf{y}} := \begin{cases} \langle \mathbf{M}, \nabla \varphi_i(\mathbf{y}) \rangle & \text{if } i \in \text{NodesOfEle}(\mathbf{y}), \\ 0 & \text{otherwise.} \end{cases} \quad (14)$$

where $\text{NodesOfEle}(\mathbf{y})$ gives the nodes of the finite element that contains the dipole.

2.3.3. Venant approach Exploiting Saint Venant's principle, we approximate a point dipole by a distribution of electrical monopoles [10, 61]. We place monopoles at the finite element node closest to the source position and those sharing an edge with this node. We adjust the charges of the monopoles so that the dipole moment of this configuration matches the dipole moment of the source as good as possible, while the sum of charges and higher moments remain zero. To avoid numerical instabilities as a consequence of huge source loads, an additional regularization is needed [10, 61]. If we denote the set of neighboring FE nodes for a dipole at position \mathbf{y} by $\text{Neighbours}(\mathbf{y})$ and the strength of the monopole at FE node $\xi_i \in \text{Neighbours}(\mathbf{y})$ by q_i , we obtain the right-hand side

$$b_i^{\mathbf{y}} := \begin{cases} -q_i & \text{if } \xi_i \in \text{Neighbours}(\mathbf{y}), \\ 0 & \text{otherwise.} \end{cases} \quad (15)$$

Table 1. Four layer sphere models used for the isotropic reference scenarios

Compartment	Outer radius	Isotropic conductivity (S/m)
Skin	92mm	0.43
Skull	88mm	0.01
CSF	80mm	1.79
Brain (adult)	76mm	0.33
Brain (child)	76mm	0.51
Brain (premature baby)	76mm	0.59

2.4. Computational efficiency

The two direct approaches Venant and PI, which approximate the dipolar source locally by a distribution of electrical monopoles, have a sparse right hand side and allow the calculation of a single solution in a few milliseconds when applying the transfer matrix approach [64]. In contrast, the subtraction approach has a much higher computational demand since both the right hand side computation (12) and also its multiplication to the transfer matrix are computationally demanding since (12) is a fully populated vector (see [16] for more details).

2.5. Quasi-analytical solution, difference criterion and electrode configuration

In [14], a quasi-analytical solution was derived for a mathematical dipole in an anisotropic multilayer sphere model that will be used here to compute modeling errors (isotropic versus anisotropic) and numerical errors (numerical versus quasi-analytical). We use the relative error (RE)

$$RE(\mathbf{u}^1, \mathbf{u}^2) := \frac{\|\mathbf{u}^1 - \mathbf{u}^2\|_2}{\|\mathbf{u}^2\|_2}$$

as a difference measure throughout our study. $\mathbf{u}^1, \mathbf{u}^2 \in \mathbb{R}^m$ with m the number of surface electrodes might, for example, denote the numerical and the quasi-analytical solutions or the forward solution in anisotropic and isotropic brain compartment models, resp..

To achieve error measures which are independent of the choice of the sensor configuration, we distribute the electrodes in a most-regular way over the outer sphere surface. In this way we generated a configuration with $m = 748$ electrodes on the surface of the outer sphere of our four layer sphere model.

2.6. Volume conductor models

Three four-layer sphere volume conductor models are used in our study, an *adult model*, a *child model* and a *premature baby model*.

Table 1 presents the radii and the conductivity parameters for the isotropic reference scenarios of the four spherical layers that approximate the compartments skin, skull,

Table 2. Conductivities in radial and tangential directions used for the anisotropic brain scenarios

Model	radial (S/m)	tangential (S/m)
Adult	0.41	0.29
Child	0.783	0.29
Premature baby	1.2	0.24

cerebrospinal fluid (CSF) and brain. While the radii of all compartments and the isotropic conductivities of the compartments skin [44], skull [13] and CSF [4] were fixed throughout our studies, the conductivity of the brain compartment differs between the three models in the isotropic (Table 1) and anisotropic (Table 2) modeling situations.

For the adult model in Table 1, we used the standard isotropic brain conductivity of $0.33S/m$ as generally used in source analysis [20, 35, 44]. Furthermore, we fixed the ratios between radial and tangential conductivities in Table 2 for the anisotropic brain models of 1.41:1 (adult), 2.7:1 (child) and 5:1 (premature baby) following the motivation given in the introduction.

The values for radial and tangential conductivity for the adult model in Table 2 were computed by means of an optimization procedure. We computed forward solutions using the quasi-analytical forward method for 16,338 dipole locations and three dipole moments in the cartesian directions, overall thus 49,014 forward solutions, first for the isotropic adult reference scenario and, in a second step, for a series of corresponding anisotropic scenarios with fixed ratio of 1.41:1 but differing magnitudes for radial and tangential conductivities. For each of those anisotropic scenarios, we summed up the RE's between isotropic and anisotropic electrode potentials over all 49,014 sources. The radial and tangential conductivity parameters with the minimal RE were then chosen as the corresponding anisotropic brain adult model as indicated in Table 2. We can therefore state that the presented effects in the results section are *anisotropy effects* and not due to suboptimally chosen conductivity values.

We now motivate the chosen optimized conductivity parameters for the child and premature baby models. The grey matter cytoarchitecture in premature babies is dominated by the apical dendrites of pyramidal cells that have few branches and are arrayed radially [34, 33]. The decrease of relative anisotropy in the grey matter compartment (in our model a decreasing anisotropy ratio from 5:1 to 2.7:1 and down to 1.41:1) was accompanied by a decrease in the average apparent diffusion coefficient values (in our model an assumed decreasing radial conductivity in Table 2 and an assumed decreasing homogenized isotropic conductivity in Table 1) when development progresses [34, 33]. The authors furthermore report that during maturation pyramidal cells elaborate highly-branched basal dendrites which tend to be arranged parallel to the cortical surface and, in addition, thalamocortical afferent fibers are added that are also oriented parallel to the cortical surface [34, 33]. We therefore assumed a slightly increasing tangential conductivity between premature baby and child model (Table 2).

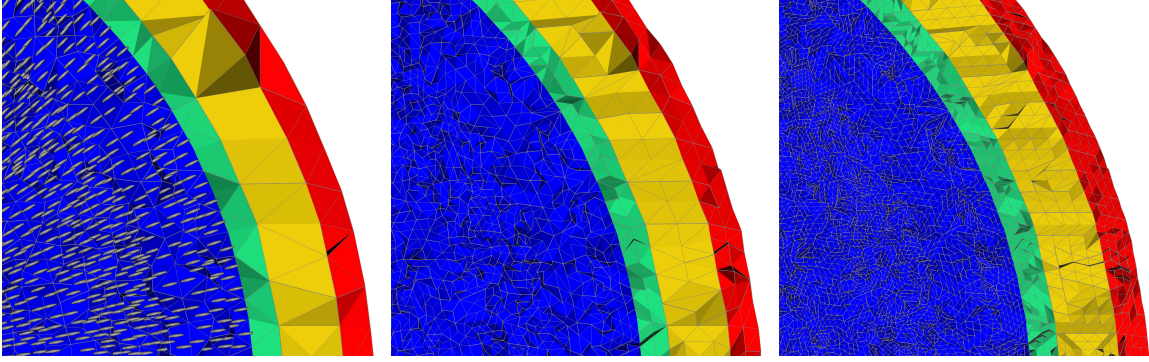


Figure 1. Visualization of the basic FE mesh *mesh142k* (left) and the globally-refined meshes *mesh1.1m* (middle) and *mesh9.5m* (right). See also Table 3.

Table 3. Globally refined tetrahedral FE meshes: Generation procedure and number of nodes and elements.

Mesh	Generated with	Nodes	Elements
mesh142k	Tetgen	142,563	900,372
mesh1.1m	Refinement	1,188,329	7,202,976
mesh9.5m	Refinement	9,590,961	57,623,808

Under these constraints, we performed again an optimization as explained for the adult model to ensure that the chosen homogenized isotropic conductivities for child and premature baby model in Table 1 have minimal RE's to their corresponding anisotropic models shown in Table 2 so that the presented effects in the results section are again *anisotropy effects* and not due to suboptimally chosen corresponding conductivity values.

2.7. Tetrahedral mesh generation

For the generation of our coarsest tetrahedral FE mesh, namely *mesh142k* (Table 3 and Figure 1), we used TetGen [49], which implements a constrained Delaunay tetrahedralization (CDT) approach [51, 50]. The meshing procedure started with the preparation of a suitable boundary discretization of the model. For each of the four layers and for a given triangle edge length, nodes were distributed in a most-regular way and connected through triangles. This yielded a valid triangular surface mesh for each of the four layers. Meshes of different layers were not intersecting each other. The CDT approach was then used to construct a tetrahedralization conforming to the surface meshes. It first built a Delaunay tetrahedralization of the vertices of the surface meshes. It then used a local degeneracy removal algorithm combining vertex perturbation and vertex insertion to construct a new set of vertices which included the input set of vertices. In the last step, a fast facet recovery algorithm was used to construct the CDT [52, 51]. This approach is combined with two further constraints to the size and

Table 4. Locally refined tetrahedral FE meshes: Generation procedure, refinement area around the fixed source location (in mm) and number of nodes and elements.

Mesh	Generated with	Ref. area around source	Nodes	Elements
mesh142k	Tetgen	0mm	142,563	900,372
mesh142k_10	Refinement	10mm	144,137	909,747
mesh142k_20	Refinement	20mm	153,325	964,809
mesh142k_30	Refinement	30mm	174,468	1,093,566
mesh142k_40	Refinement	40mm	211,729	1,315,947
mesh142k_50	Refinement	50mm	266,499	1,646,015
mesh142k_60	Refinement	60mm	339,627	2,087,099
mesh142k_70	Refinement	70mm	430,432	2,634,985
mesh142k_100	Refinement	100mm	774,189	4,710,009
mesh1.1m	Refinement	globally refined	1,188,329	7,202,976

shape of the tetrahedra. The first constraint can be used to restrict the volume of the generated tetrahedra in a certain compartment, the so-called *volume constraint*. The second constraint is important for the generation of quality tetrahedra. If R denotes the radius of the unique circumsphere of a tetrahedron and L its shortest edge length, the so-called radius-edge ratio of the tetrahedron can be defined as $Q = \frac{R}{L}$. The radius-edge ratio can detect almost all badly-shaped tetrahedra except one type of tetrahedra, so-called slivers. A sliver is a very flat tetrahedron which has no small edges, but can have arbitrarily large dihedral angles (close to π). For this reason, an additional mesh smoothing and optimization step was used to remove the slivers and improve the overall mesh quality.

Based upon *mesh142k*, we created further globally and locally refined meshes. Refinement is carried out using regular refinement which splits every tetrahedron of the mesh in eight new tetrahedra [7, 6]. The specialty of this approach is that the set of nodes of the coarser meshes are a subset of the nodes of each finer mesh, needed later for maintaining the homogeneity condition of the subtraction approach. In this way, two regularly and globally refined meshes were created (Table 3 and Figure 1). Furthermore, we are interested in the effect of local in comparison to global mesh refinement. Therefore, we fixed the source at

$$(183.044; 169.393; 149.969)^T$$

having a distance of 73.93mm to the midpoint and of 2.07mm to the CSF. We then refined *mesh142k* inside a given radius around this position. First, a regular refinement, also called *red refinement*, of each tetrahedron inside the radius is applied. Secondly, in the *green refinement*, a closure is created so that the locally refined mesh has no hanging nodes [7, 6] (Table 4). We refine only *mesh142k* and denote the locally refined meshes

with $mesh142k_x$ whereby x is the radius of the refinement area around the dipole. For example, if we refine all tetrahedra that lie in at most 10mm distance to the fixed position, we denote the corresponding model $mesh142k_10$.

For $mesh142k$, the conductivity tensors indicated in Tables 1 and 2 were then computed in the barycenters of the elements. First, with regard to the studies in the results-sections 3.1 and 3.2, where we want to maintain the homogeneity condition for the subtraction approach, we assigned the conductivity of the original tetrahedron to each of the eight new tetrahedra in the refinement, that is, we accept that the refinement will only improve the FE approximation, while the model error is not reduced. Secondly, for the study in results-section 3.3, we calculate adapted conductivity tensors for the refined meshes, that is, we obtain meshes where also the conductivity tensors of the refined brain elements change from element to element.

2.8. Dipole positions

Dipoles were positioned in the brain compartment between the radii 68mm and 75mm, that is, in a distance of minimally 1mm and maximally 8mm to the CSF (the next bigger change in conductivity). We chose this intervall, because it is well-known that numerical errors increase with decreasing distance of the source to the next bigger conductivity jump (i.e., the CSF) and a mathematical reasoning for this phenomenon was given in [65]. We thus used on purpose a source space intervall where we have to be aware of bigger numerical forward modeling errors [65, 16, 28]. 10 different dipole positions were chosen randomly in each of the seven (68-69mm,...,74-75mm) 1mm intervals, that is, altogether 70 different source positions. Sources were placed in the barycenters of elements of $mesh142k$. Numerical errors were shown to be minimal for sources in element barycenters for both subtraction and PI approaches, while for the Venant approach, best source positions are the FE nodes [57]. Since these errors are on an overall low scale [57], our choice is slightly in favor of the subtraction and PI approaches. Since normally-oriented dipoles in the grey matter compartment are the anatomically and physiologically realistic sources in combination with the used radial conductivity anisotropy, we mainly only present results for radially-oriented sources. However, for academic interest, we also present one result figure for tangentially-oriented sources.

2.9. Computational platform and used software

All simulations ran on an IBM server with 2 Xeon X5650 processors (2.67 GHz) using the SimBio software environment [53].

3. Results

For studies 3.1 and 3.2, the refined mesh models are constrained to fulfill the homogeneity condition of the full subtraction approach. The studies have the goal to present the effect of cortical conductivity anisotropy in the three different volume

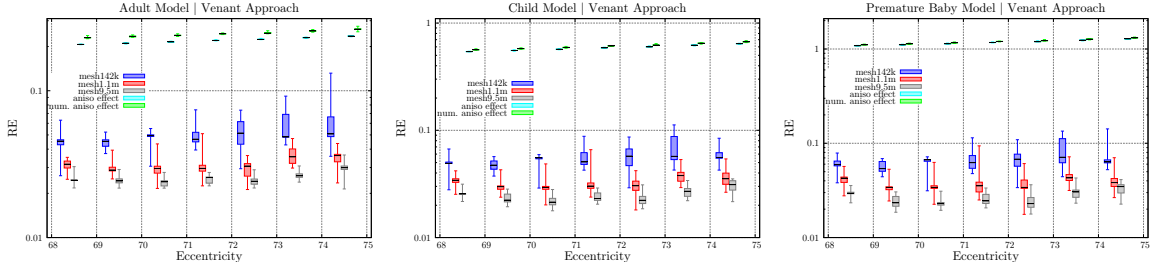


Figure 2. RE for normally-oriented sources and the Venant FE approach for *adult* (left column), *child* (middle column) and *premature baby* (right column) model: Boxplots are shown for the effect of cortical anisotropy (cyan), for the numerical anisotropy effect (green) (see description in 3.1) and for the numerical errors in the coarsest *mesh142k* (blue) and the once (*mesh1.1m*, red) and twice (*mesh9.5m*, grey) refined meshes.

conductor models, relate those effects to the numerical errors and determine the FEM approach that overall performs best. In the last study 3.3, the model error is further reduced by means of relaxing the homogeneity condition, and the best-performing FEM approach of studies 3.1 and 3.2 is used for computation.

For the presentation of our results we use boxplots.

Volume conductor model (*adult*, *child* or *premature baby*, see 2.6) and the FE dipole modeling approach (Venant, PI or subtraction, see 2.3) are denoted in the title of each figure. The x-axis shows source eccentricity and the y-axis the used error measure.

3.1. Globally refined meshes that fulfill the homogeneity condition

Figures 2 and 3 show the RE results for normally-oriented sources, for different volume conductor models and different dipole modeling approaches. The figures contain

- the effect of cortical anisotropy (*aniso effect*, cyan), that is, the comparison between quasi-analytical forward results in the anisotropic and in the corresponding isotropic volume conductor model (see 2.6, Tables 1 and 2),
- the numerical anisotropy effect (*num. aniso effect*, green), defined here as the results of the Venant approach in *mesh9.5m* for isotropic conductivities versus the quasi-analytical results in the corresponding anisotropic model and
- the numerical errors of the three different FE approaches in the coarsest *mesh142k* and in the once (*mesh1.1m*) and twice (*mesh9.5m*) refined meshes, that is, the numerical forward modeling results versus the quasi-analytical results, both for anisotropic conductivity in the cortex.

Figure 2 presents those results for the Venant approach and for the *adult* model (left), for the *child* model (middle) and for the *premature baby* model (right). The *aniso effect* (cyan) is increasing proportionally to the degree of cortical anisotropy in the model, that is, it increases from the *adult* (in intervall 68-69mm, an RE median of 0.2067) to the *premature baby* model (an RE median of 1.0821). As expected, the

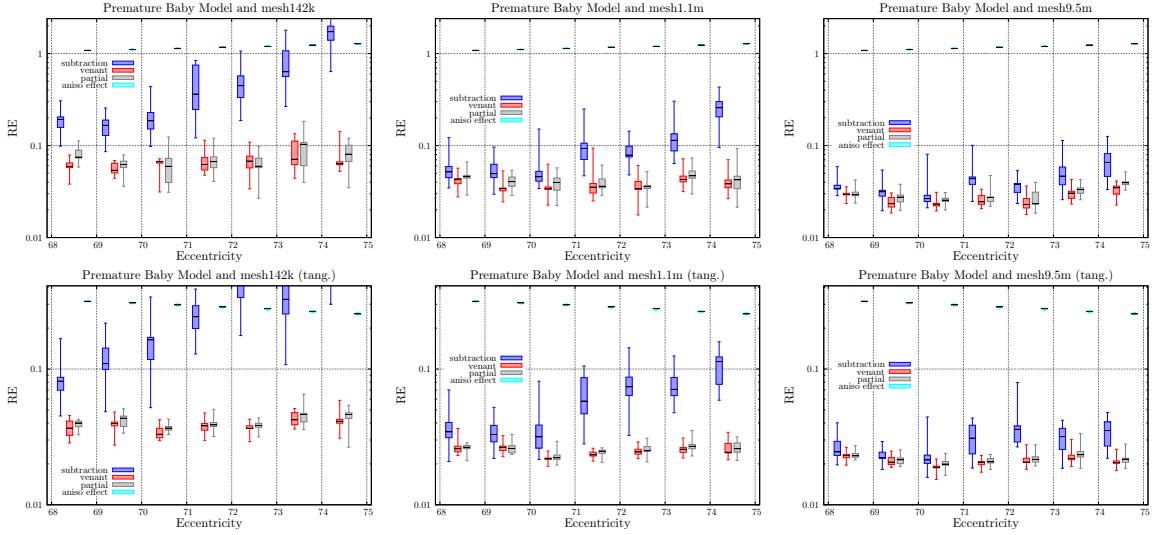


Figure 3. RE for normally-oriented (upper row) and tangentially-oriented (lower row) sources for the *premature baby* model for the coarsest *mesh142k* (left column) and the once (*mesh1.1m*, middle column) and twice (*mesh9.5m*, right column) refined meshes. Boxplots are shown for the effect of cortical anisotropy (cyan) and for the numerical errors for subtraction (blue), Venant (red) and partial integration (grey) approach.

num. aniso effect (green) closely follows the *aniso effect*, only on a slightly higher error scale, which shows that the error is mainly due to ignoring cortical anisotropy, while the additional numerical error is small. Most importantly, for *mesh142k* (blue), *mesh1.1m* (red) and *mesh9.5m* (grey) we obtain a clear convergence behaviour, that is, the numerical errors are still significant for the coarsest *mesh142k*, while for the finest mesh *mesh9.5m* they are in the area of $0.01 \leq \text{RE} \leq 0.04$ and thus far below the *aniso effect*.

Figure 3 shows a direct comparison of the three FE approaches subtraction (blue), Venant (red) and partial integration (grey) in *mesh142k* (left column), *mesh1.1m* (middle column) and *mesh9.5m* (right column) for both normally-oriented (upper row) as well as tangentially-oriented (lower row) sources in the *premature baby* model. All three approaches show a clear convergence behavior with increasing mesh size. However, it is clearly visible that although the subtraction is by far the most computationally expensive FE approach and although we chose source positions in favor of the subtraction (and the PI) approach, it shows highest numerical errors for all three meshes. Both Venant and PI approach are at about the same error level with a slight advantage of the Venant approach, even if source positions were chosen in favor of the PI.

3.2. Locally refined meshes that fulfill the homogeneity condition

In the second study, we focus our interest on the numerical RE errors in the locally-refined meshes around the fixed source position as described in 2.7 (see, especially Table 4). Table 5 shows the results for all three dipole models and for normally- and

Table 5. Relative error (RE) for all three dipole models and locally refined meshes.

Model	normally-oriented sources			tangentially-oriented sources		
	sub.	venant	partial	sub.	venant	partial
mesh142k	0.16899	0.07985	0.10579	0.09028	0.04279	0.04030
mesh142k_10	0.16844	0.07979	0.09093	0.09034	0.04286	0.04049
mesh142k_20	0.17036	0.07861	0.08995	0.09112	0.04446	0.04191
mesh142k_30	0.18633	0.07101	0.07591	0.13560	0.03878	0.03075
mesh142k_40	0.05510	0.04554	0.04650	0.05632	0.02629	0.02507
mesh142k_50	0.06458	0.04153	0.04306	0.03438	0.02540	0.02354
mesh142k_60	0.06310	0.04132	0.04284	0.03377	0.02530	0.02318
mesh142k_70	0.06205	0.04154	0.04303	0.03578	0.02523	0.02305
mesh142k_100	0.06124	0.04198	0.04348	0.03354	0.02492	0.02278
mesh1.1m	0.06048	0.04202	0.04344	0.03278	0.02492	0.02275

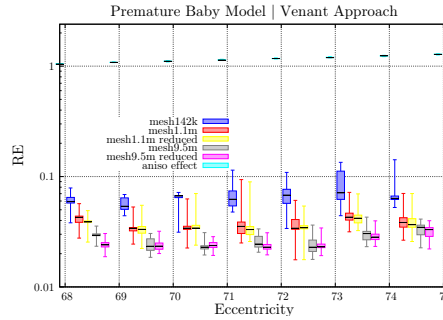


Figure 4. RE for normally-oriented sources and the Venant FE approach for the *premature baby* model and adapted conductivities: Boxplots are shown for the effect of cortical anisotropy (cyan) and for the numerical errors in the coarsest *mesh142k* (blue) and the once (*mesh1.1m*, red) and twice (*mesh9.5m*, grey) refined meshes without adapted conductivities from study 3.1 and for the once (*mesh1.1m reduced*, yellow) and twice (*mesh9.5m reduced*, pink) refined meshes with adapted conductivities.

tangentially-oriented sources. While the dipole has a distance of 18.07mm to the surface of the multisphere model, we observe a clear error decrease for a radius of 40mm and nearly no more improvement for further refinement. Nearly the same numerical accuracy could have thus been achieved with less than one fifth of the FE nodes. Table 5 confirms that the subtraction approach can not compete against the direct approaches Venant and PI and, when taking into account that the source position was chosen in the element barycenter, that is, in favor of the PI approach, we can conclude again that the Venant approach seems to be the best choice out of the three tested FE approaches.

3.3. Globally refined meshes with adapted conductivities

For the last study, we will only use the best performing FE approach from studies 3.1 and 3.2, namely the Venant FE approach, and the model with highest cortical anisotropy, the premature baby model. The results of the last simulation study are shown in Figure 4. The presented boxplots for the *aniso effect* (cyan) and for *mesh142k* (blue) as well as for *mesh1.1m* (red) and *mesh9.5m* (grey) are the known numerical accuracy results for the globally-refined meshes from study 3.1, that is, *mesh1.1m* and *mesh9.5m* fulfill the homogeneity condition. Additionally, we present the results in *reduced mesh1.1m* (yellow) and *reduced mesh9.5m* (pink), where the homogeneity condition was relaxed, that is, where the conductivities in the refined models were adapted to the real model. A comparison of the results *mesh1.1m* versus *reduced mesh1.1m* and *mesh9.5m* versus *reduced mesh9.5m* shows only a slight overall RE numerical error decrease for the two adapted models. The slight improvements in the modeling of the cortical conductivities thus does not show a significant improvement with regard to the numerical errors.

4. Discussion and conclusion

In this paper, we studied the effect of cortical conductivity anisotropy versus modeling and numerical errors of three different FE approaches for the EEG forward problem, namely the subtraction, the partial integration (PI) and the Venant approach. To do so, we used multi-layer sphere volume conductors and examined maximal cortical conductivity anisotropy for three different scenarios, reflecting the increasing anisotropy ratios from an *adult* over a *child* to a *premature baby* modeling situation. We assumed maximal anisotropy ratios of 1.41:1, 2.7:1 and 5:1, resp., as motivated by the measurements of [48, 34, 33].

We used a relative error (RE) based optimization procedure to find the best-approximating conductivity parameters for the isotropy-anisotropy pairs that were compared. This procedure allows us to state that the presented RE-effects are due to cortical anisotropy and not due to suboptimally chosen conductivity values. For other choices of the conductivities, the RE-errors would thus even be larger.

We showed that cortical conductivity anisotropy has a significant effect on the forward EEG problem and should thus be modeled. The effect increased with increasing anisotropy ratio so that the significance of modeling it increases with decreasing age of the studied subjects. Since the investigation of the cortical development is of high interest [17, 45], a correct modeling of source space anisotropy might thus significantly contribute to an understanding of cortical maturation effects. Realistic measurement of grey matter conductivity anisotropy can be performed using a combination of newest MRI technology [25, 11] and the linear effective medium approach model for relating water diffusion and conductivity [54, 36, 58], so that the application of the proposed and evaluated methodology to realistic situations seems straightforward.

In our first two studies, we used globally- and locally-refined meshes that fulfilled

the so-called *homogeneity condition*. This condition is important for the subtraction approach, where the mathematical theory suggests that a sufficiently (*sufficient* relative to the mesh resolution) large neighborhood around the source position with constant conductivity is needed for an appropriate treatment of the source singularity [65, 16]. In isotropically conducting brain compartments, this can be easily and well fulfilled [65, 16], but the situation is more complicated in volume conductors with anisotropic grey matter conductivity, as evaluated for the first time in this paper. We found that the smaller the neighborhood (note that a smaller neighborhood offers the possibility of reducing the model error by means of adapting the conductivities), the larger the numerical errors of the subtraction approach, resulting in larger overall errors. As a consequence, for the subtraction approach, we found that it is better not to adapt conductivity tensors in refined areas around the source. While the subtraction approach is very sensitive to this condition, it is of less importance for both direct approaches PI and Venant, so that the performance of those approaches could even slightly (even though, in our study with the chosen parameters, not significantly) be improved (see study 3.3). This effect was only small, since the elements in the grey matter compartment were already relatively small for *mesh142k*, so that already the coarsest mesh captured the real conductivity structure in the volume conductor quite well. More importantly, we showed FE convergence for all three FE approaches, so that all of them are appropriate methods for the modeling of source space anisotropy. Relative errors (RE) were shown to be far below anisotropy effect errors, especially for the highest FE resolutions. We also investigated the relative difference measure (RDM) and the magnification factor (MAG) [31] and found that the RE errors decomposed into both of them with, however, a more distinct MAG component. In our study with the chosen meshes, we found the Venant approach to be the overall best-performing method with regard to accuracy, computational complexity and practicability. We can thus state that cortical anisotropy should be modeled and, from the results of this study, the Venant FE approach should be used for it.

In study 3.2, we showed that for accurate FE modeling, mesh-refinement is not only needed around the source, but between the source and those EEG sensors, that capture the main source activity. Since we did not observe an error reduction for larger refinement radii, we can also conclude that in areas far away from the source (for superficial sources, e.g., deeper areas in the brain), coarser mesh resolutions seem sufficient to reduce computational complexity. However, since our FEM approach is completely linear in the number of nodes [64], even high resolutions are practicable, as shown in this study, where the finest resolution had nearly 10 Million FE nodes.

Finally, we would like to mention that from our former experience when using realistic head models [23, 62, 63] and from the results of this study, we expect that the proposed modeling is not only relevant for EEG, but also for MEG, and, because of the higher anisotropy ratios, especially for modeling of newborn MEG [39, 37, 40, 27] and fetal MEG [17, 41].

Acknowledgment

This work was supported by the Deutsche Forschungsgemeinschaft (WO1425/3-1, GR3179/3-1, HA2899/14-1).

References

- [1] C.R. Almli, M.J. Rivkin, and R.C. McKinstry. The NIH MRI study of normal brain development (objective-2): newborns, infants, toddlers, and preschoolers. *Neuroimage*, 35:308–325, 2007.
- [2] K.A. Awada, D.R. Jackson, J.T. Williams, D.R. Wilton, S.B. Baumann, and A.C. Papanicolaou. Computational aspects of finite element modeling in EEG source localization. *IEEE Trans Biomed. Eng.*, 44(8):736–751, 1997.
- [3] P.J. Basser, D. Le Bihan, and J. Mattiello. Estimation of the effective self-diffusion-tensor from the NMR spin echo. *J. Magn. Res. B*, 103:247–254, 1994.
- [4] S.B. Baumann, D.R. Wozny, S.K. Kelly, and F.M. Meno. The electrical conductivity of human cerebrospinal fluid at body temperature. *IEEE Trans Biomed. Eng.*, 44(3):220–223, 1997.
- [5] O. Bertrand, M. Thévenet, and F. Perrin. 3D finite element method in brain electrical activity studies. In J. Nenonen, H.M. Rajala, and T. Katila, editors, *Biomagnetic Localization and 3D Modelling*, pages 154–171. Report of the Dep. of Tech.Physics, Helsinki University of Technology, 1991.
- [6] J. Bey. Tetrahedral grid refinement. *Computing*, 55:355–378, 1995. 10.1007/BF02238487.
- [7] J. Bey. *Finite-Volumen- und Mehrgitter-Verfahren für elliptische Randwertprobleme*. Teubner Verlag, 1998.
- [8] D. Braess. *Finite Elements: Theory, Fast Solvers and Applications in Solid Mechanics*. Cambridge University Press, 2007.
- [9] R. Brette and A. Destexhe. *Handbook of Neural Activity Measurement*. Cambridge University Press, 2012.
- [10] H. Buchner, G. Knoll, M. Fuchs, A. Rienäcker, R. Beckmann, M. Wagner, J. Silny, and J. Pesch. Inverse localization of electric dipole current sources in finite element models of the human head. *Electroenc. Clin. Neurophysiol.*, 102:267–278, 1997.
- [11] J. Cohen-Adad, J.R. Polimeni, K.G. Helmer, T. Benner, J.A. McNab, L.L. Wald, B.R. Rosen, and C. Mainero. T_2^* mapping and B_0 orientation-dependence at 7T reveal cyto- and myeloarchitecture organization of the human cortex. *NeuroImage*, 60:1006–1014, 2012.
- [12] M.J.D. Cook and Z.J. Koles. The effect of tissue anisotropy on the EEG inverse problem. In *Proc. of the 30th Annual Int. Conf. of the IEEE Engineering in Medicine and Biology Society, Vancouver, British Columbia, Canada, August 20-24*, pages 4563–4566, 2008.
- [13] M. Dannhauer, B. Lanfer, C.H. Wolters, and T.R. Knösche. Modeling of the human skull in EEG source analysis. *Human Brain Mapping*, 32(9):1383–1399, 2011. DOI: 10.1002/hbm.21114, PMID: 20690140.
- [14] J.C. de Munck and M. Peters. A fast method to compute the potential in the multi sphere model. *IEEE Trans Biomed. Eng.*, 40(11):1166–1174, 1993.
- [15] J.C. de Munck, B.W. van Dijk, and H. Spekreijse. Mathematical dipoles are adequate to describe realistic generators of human brain activity. *IEEE Trans Biomed. Eng.*, 35(11):960–966, 1988.
- [16] F. Drechsler, C.H. Wolters, T. Dierkes, H. Si, and L. Grasedyck. A full subtraction approach for finite element method based source analysis using constrained delaunay tetrahedralisation. *NeuroImage*, 46(4):1055–1065, 2009. <http://dx.doi.org/10.1016/j.neuroimage.2009.02.024>, PMID: 19264145.
- [17] H. Eswaran, J. Wilson, H. Preissl, S. Robinson, J. Vrba, P. Murphy, D. Rose, and C. Lowery. Magnetoencephalographic recordings of visual evoked brain activity in the human fetus. *Lancet*, 360:779–780, 2002.

- [18] D. Güllmar, J. Haueisen, and J.R. Reichenbach. Influence of anisotropic electrical conductivity in white matter tissue on the EEG/MEG forward and inverse solution. a high-resolution whole head simulation study. *NeuroImage*, 2010. doi:10.1016/j.neuroimage.2010.02.014.
- [19] W. Hackbusch. *Elliptic Differential Equations. Theory and Numerical Treatment*. Springer-Verlag, Berlin, 1992.
- [20] H. Hallez, B. Vanrumste, P. Van Hese, Y. D’Asseler, I. Lemahieu, and R. Van de Walle. A finite difference method with reciprocity used to incorporate anisotropy in electroencephalogram dipole source localization. *Phys.Med.Biol.*, 50:3787–3806, 2005.
- [21] H. Hallez, B. Vanrumste, P. Van Hese, S. Delputte, and I. Lemahieu. Dipole estimation errors due to differences in modeling anisotropic conductivities in realistic head models for EEG source analysis. *Phys.Med.Biol.*, 53:1877–1894, 2008.
- [22] M.S. Hämäläinen, R. Hari, R. Ilmoniemi, J. Knuutila, and O. Lounasmaa. Magnetoencephalography: theory, instrumentation, and applications to noninvasive studies of the working human brain. *Rev.Mod.Phys.*, 65:413–497, 1993.
- [23] J. Haueisen, C. Ramon, H. Brauer, and H. Nowak. The influence of local conductivity changes on MEG and EEG. *Biomedizinische Technik*, 45(7-8):211–214, 2000.
- [24] J. Haueisen, D.S. Tuch, C. Ramon, P.H. Schimpf, V.J. Wedeen, J.S. George, and J.W. Belliveau. The influence of brain tissue anisotropy on human EEG and MEG. *NeuroImage*, 15:159–166, 2002.
- [25] R.M. Heidemann, D.A. Porter, A. Anwender, T. Feiweier, K. Heberlein, T. Knösche, and R. Turner. Diffusion imaging in humans at 7T using readout-segmented EPI and GRAPPA. *Magnetic Resonance in Medicine*, 64(1):9–14, 2010.
- [26] D.K. Jones. *Diffusion MRI: Theory, Methods, and Applications*. Oxford University Press, USA, ISBN-13: 9780195369779, December 2010.
- [27] S. Lew, M. Hämäläinen, C.H. Wolters, D.D. Silva, M.-S. Choe, E. Grant, and Y. Okada. Effect of the fontanel on MEG and EEG source analysis using a finite element model of an infant head. In *Human Brain Mapping, Quebec City, Canada, June 26-30*, <http://www.humanbrainmapping.org/hbm2011/>, 2011.
- [28] S. Lew, C.H. Wolters, T. Dierkes, C. Röer, and R.S. MacLeod. Accuracy and run-time comparison for different potential approaches and iterative solvers in finite element method based EEG source analysis. *Applied Numerical Mathematics*, 59(8):1970–1988, 2009. NIHMSID 120338, PMCID: PMC2791331.
- [29] F. Lucka, S. Pursiainen, M. Burger, and C.H. Wolters. Hierarchical bayesian inference for the EEG inverse problem using realistic FE head models: Depth localization and source separation for focal primary currents. *NeuroImage*, 61(4):1364 – 1382, 2012.
- [30] G. Marin, C. Guerin, S. Baillet, L. Garnero, and Meunier G. Influence of skull anisotropy for the forward and inverse problem in EEG: simulation studies using the FEM on realistic head models. *Human Brain Mapping*, 6:250–269, 1998.
- [31] J.W.H. Meijs, O.W. Weier, M.J. Peters, and A. van Oosterom. On the numerical accuracy of the boundary element method. *IEEE Trans Biomed. Eng.*, 36:1038–1049, 1989.
- [32] L. Mrzljak, H.B. Uylings, I. Kostovic, and C.G. Van Eden. Prenatal development of neurons in the human prefrontal cortex: I. a qualitative golgi study. *J Comp Neurol*, 271(3):355–386, 1988.
- [33] J. Neil, J. Miller, P. Mukherjee, and P. S. Hüppi. Diffusion tensor imaging of normal and injured developing human brain - a technical review. *NMR in Biomedicine*, 15:543–552, 2002.
- [34] J.J. Neil, R.C. McKinstry, B.L. Schlaggar, G. Schefft, S.I. Shiran, J.S. Shimony, A.Z. Snyder, C.R. Almli, E. Akbudak, and T.E. Conturo. Evaluation of diffusion anisotropy during human cortical grey matter development. In *Proceedings of ISMRM, 8th Annual Meeting and Exhibition*, page 591, 2000.
- [35] L.A. Neilson, M. Kovalyovc, and Z.J. Koles. A computationally efficient method for accurately solving the EEG forward problem in a finely discretized head model. *Clin.Neurophysiol.*, 116:2302–2314, 2005.

- [36] S.H. Oh, S.Y. Lee, M.H. Cho, T.-S. Kim, and I.H. Kim. Electrical conductivity estimation from diffusion tensor and t2: a silk yarn phantom study. In *Proc.Intl.Soc.Mag.Reson.Med.*, volume 14, page 3034, 2006.
- [37] Y. Okada, K. Pratt, C. Atwood, A. Mascarenas, R. Reineman, J. Nurminen, and D. Paulson. Babysquid: a mobile, high-resolution multichannel MEG system for neonatal brain assessment. *Rev. Sci. Instrum.*, 77:24301–24309, 2006.
- [38] J. Ollikainen, M. Vauhkonen, P.A. Karjalainen, and J.P. Kaipio. Effects of local skull inhomogeneities on EEG source estimation. *Med.Eng.Phys.*, 21:143–154, 1999.
- [39] E. Pihko, L. Lauronen, H. Wikstrom, S. Taulu, J. Nurminen, S. Kivitie-Kallio, and Y. Okada. Somatosensory evoked potentials and magnetic fields elicited by tactile stimulation of the hand during active and quiet sleep in newborns. *Clin Neurophysiol*, 115:448–455, 2004.
- [40] E. Pihko, P. Nevalainen, J. Stephen, Y. Okada, and L. Lauronen. Maturation of somatosensory cortical processing from birth to adulthood revealed by magnetoencephalography. *Clin Neurophysiol*, 120:1552–1561, 2009.
- [41] H. Preissl, C.L. Lowery, and H. Eswaran. Fetal magnetoencephalography: current progress and trends. *Exp Neurol.*, 190(Suppl 1):S28–36, 2004.
- [42] S. Pursiainen. Raviart-thomas-type sources adapted to applied EEG and MEG: implementation and results. *Inverse Problems*, 28:16pp., 2012.
- [43] S. Pursiainen, A. Sorrentino, C. Campi, and M. Piana. Forward simulation and inverse dipole localization with the lowest order raviart-thomas elements for electroencephalography. *Inverse Problems*, 27(4), 2011.
- [44] C. Ramon, P. Schimpf, and J. Haueisen. Influence of head models on EEG simulations and inverse source localizations. *BioMedical Engineering OnLine*, 5(10), 2006.
- [45] N. Roche-Labarbe, A.Aarabi, G. Kongolo, C. Gondry-Jouet, M. Dümpelmann, R. Grebe, and F. Wallois. High-resolution electroencephalography and source localization in neonates. *Human Brain Mapping*, 29:167–176, 2008.
- [46] J. Sarvas. Basic mathematical and electromagnetic concepts of the biomagnetic inverse problem. *Phys.Med.Biol.*, 32(1):11–22, 1987.
- [47] P.H. Schimpf, C.R. Ramon, and J. Haueisen. Dipole models for the EEG and MEG. *IEEE Trans Biomed. Eng.*, 49(5):409–418, 2002.
- [48] J. S. Shimony, R.C. McKinstry, E. Akbudak, J.A. Aronovitz, A.Z. Snyder, N.F. Lori, T.S. Cull, and T.E. Conturo. Quantitative diffusion-tensor anisotropy brain MR imaging: Normative human data and anatomic analysis. *Radiology*, 212(3):770–784, 1999.
- [49] H. Si. TetGen, a quality tetrahedral mesh generator and three-dimensional delaunay triangulator, v1.3, user’s manual. Technical Report 9, Weierstrass Institute for Applied Analysis and Stochastics, 2004. <http://tetgen.berlios.de>.
- [50] H. Si. TetView. <http://tetgen.berlios.de/tetview.html>, 2007.
- [51] H. Si. Adaptive tetrahedral mesh generation by constrained Delaunay refinement. *International Journal for Numerical Methods in Engineering*, 75(7):856–880, 2008.
- [52] H. Si and K. Gärtner. Meshing piecewise linear complexes by constrained Delaunay tetrahedralizations. In *Proc. 14th International Meshing Roundtable*, pages 147–163. Sandia National Laboratories, 2005.
- [53] SimBio Development Group. SimBio: A generic environment for bio-numerical simulations. online, <https://www.mrt.uni-jena.de/simbio>, accessed June 15, 2012.
- [54] D.S. Tuch, V.J. Wedeen, A.M. Dale, J.S. George, and J.W. Belliveau. Conductivity tensor mapping of the human brain using diffusion tensor MRI. *Proc.Natl.Acad.Sci.USA*, 98(20):11697–11701, 2001.
- [55] S. Vallaghé and T. Papadopoulos. A trilinear immersed finite element method for solving the electroencephalography forward problem. *SIAM J. Sci. Comput.*, 32(4):2379–2394, 2010.
- [56] S.P. van den Broek. *Volume Conduction Effects in EEG and MEG*. PhD thesis, Proefschrift Universiteit Twente Enschede, The Netherlands, 1997.

- [57] J. Vorwerk. Comparison of numerical approaches to the EEG forward problem. Diploma thesis in Mathematics, Institut für Biomagnetismus und Biosignalanalyse, Westfälische Wilhelms-Universität Münster, april 2011.
- [58] K. Wang, J. Li, S. Zhu, B. Mueller, K. Lim, Z. Liu, and B. He. A new method to derive white matter conductivity from diffusion tensor MRI. *IEEE Trans. Biomed. Eng.*, 55(10):2481–2486, 2008.
- [59] D. Weinstein, L. Zhukov, and C. Johnson. Lead-field bases for electroencephalography source imaging. *Annals of Biomed.Eng.*, 28(9):1059–1066, 2000.
- [60] K. Wendel, N.G. Narra, M. Hannula, P. Kauppinen, and J. Malmivuo. The influence of CSF on EEG sensitivity distributions of multilayered head models. *IEEE Trans. Biomed. Eng.*, 55(4):1454–1456, 2008.
- [61] C.H. Wolters, A. Anwander, G. Berti, and U. Hartmann. Geometry-adapted hexahedral meshes improve accuracy of finite element method based EEG source analysis. *IEEE Trans.Biomed.Eng.*, 54(8):1446–1453, 2007.
- [62] C.H. Wolters, A. Anwander, X. Tricoche, S. Lew, and C.R. Johnson. Influence of local and remote white matter conductivity anisotropy for a thalamic source on EEG/MEG field and return current computation. *Int.Journal of Bioelectromagnetism*, 7(1):203–206, 2005.
- [63] C.H. Wolters, A. Anwander, D. Weinstein, M. Koch, X. Tricoche, and R.S. MacLeod. Influence of tissue conductivity anisotropy on EEG/MEG field and return current computation in a realistic head model: A simulation and visualization study using high-resolution finite element modeling. *NeuroImage*, 30(3):813–826, 2006.
- [64] C.H. Wolters, L. Grasedyck, and W. Hackbusch. Efficient computation of lead field bases and influence matrix for the FEM-based EEG and MEG inverse problem. *Inverse Problems*, 20(4):1099–1116, 2004.
- [65] C.H. Wolters, H. Köstler, C. Möller, J. Härtlein, L. Grasedyck, and W. Hackbusch. Numerical mathematics of the subtraction method for the modeling of a current dipole in EEG source reconstruction using finite element head models. *SIAM J. on Scientific Computing*, 30(1):24–45, 2007.